Nanoscale

ROYAL SOCIETY
OF CHEMISTRY

PAPER
Mohammad Arjmand *et al.*
Liquid-templated graphene aerogel electromagnetic traps

NCNST

PAPER

Check for updates

Liquid-templated graphene aerogel electromagnetic traps†

Seyyed Alireza Hashemi,‡[a] Ahmadreza Ghaffarkhah,‡[a,b] Farhad Ahmadijokani,[a,b] Hatef Yousefian,[a] Sameer E. Mhatre,[b] Anna Sinelshchikova,[c] Gabriel Banvillet,[b] Milad Kamkar, [iD][d] Orlando J. Rojas, [iD][b] Stefan Wuttke [iD][c,e] and Mohammad Arjmand [iD] *[a]

For decades, the inherently reflective nature of metallic electromagnetic (EM) shields and their induced secondary EM pollution have posed significant challenges for sensitive electronics. While numerous efforts have been made to develop superior EM shielding systems, the issue of reflection dominancy in metallic substrates remains unresolved. Herein, we addressed this long-lasting obstacle by pairing metallic shields with ultra-lightweight (density of 3.12–3.40 mg cm^{-3}) elastic anti-reflection aerogels, altering their shielding mechanism from dominant reflection (reflectance >0.8) to absorption (absorbance >0.7) by trapping EM waves inside the aerogel. The aerogel EM traps were generated using interfacial complexation, yielding engineerable filamentous liquid structures. These served as templates for aerogel creation through a follow-up process of freezing and lyophilization. The engineerable lossy medium of aerogels benefits from a multi-scale porous construct with the combined action of dielectric and conduction losses, highly dissipating the EM waves and minimizing the reflections. Notably, declining the diameter of aerogel filaments promoted its absorption dominancy, rendering it a potent dissipating medium for EM waves. Pairing a metallic substrate with filamentous aerogel EM traps has resulted in an exceptionally effective absorption-dominant shielding system, achieving absorbance levels between 0.70–0.81. This system offers a shielding effectiveness of 53–89 dB within the X-band frequency range. This innovation addresses a persistent issue in shielding science related to the reflective characteristics of metallic substrates, effectively inhibiting their induced EM reflections.

1. Introduction

Electromagnetic (EM) waves have been foundational to the evolution of human civilization's communication and cutting-edge technologies, revolutionizing sectors like aviation, education, entertainment, and therapeutics.[1] The proliferating usage of EM waves in communication and portable electronic devices has caused an increasing rate of EM interference (EMI) or EM pollution, obstructing the proper performance of sensitive electronics and adversely affecting biological entities.[1,2] Since identifying the adverse effect of EM pollution on electronic systems, many types of superconductive metallic shields have been used to mitigate the impact of EM waves.[3] Despite the high shielding effectiveness of metallic shields, their reflection-dominant shielding mechanism and the associated secondary EM pollution restrict their applicability.[1] The induced reflections as a result of enforced oscillation of free-charge carriers on the surface of highly conductive metallic substrates cause a scattered field in the form of reflection that is as harmful as the incident EM waves.[4] This restricted the applicability of metallic substrates and motivated scientists to fabricate alternative advanced EM waves absorbing materials such as carbonaceous nanomaterials,[5] conductive polymers,[6,7] and 2D MXene nanosheets[8,9] assembled in porous frameworks or embedded in polymeric blends.[10] Despite significant advancements, numerous contemporary shielding systems still predominantly depend on reflection, posing unresolved challenges due to secondary EM pollution.[1]

[a]Nanomaterials and Polymer Nanocomposites Laboratory, School of Engineering, University of British Columbia, Kelowna, BC, V1V 1V7, Canada.
E-mail: mohammad.arjmand@ubc.ca

[b]Bioproducts Institute, Department of Chemical & Biological Engineering, Department of Chemistry and Department of Wood Science, 2360 East Mall, The University of British Columbia, Vancouver, BC V6T 1Z3, Canada

[c]Basque Centre for Materials, Applications & Nanostructures (BCMaterials), Bld. Martina Casiano, 3rd. Floor UPV/EHU Science Park Barrio Sarriena s/n, Leioa, 48940, Spain

[d]Department of Chemical Engineering, Waterloo Institute for Nanotechnology, University of Waterloo, 200 University Avenue West, Waterloo, Ontario N2L 3G1, Canada

[e]Ikerbasque, Basque Foundation for Science, Bilbao, 48009, Spain

†Electronic supplementary information (ESI) available. See DOI: https://doi.org/10.1039/d3nr06478f

‡These authors equally contributed to the preparation of this assay.

Fabricating absorption-dominant shielding frameworks and trapping the incident or reflected EM waves require a target-oriented approach that can engineer the multi-scale porosities and enhance the EM waves dissipating factors, *e.g.*, multiple internal scatterings and dielectric, magnetic, and conduction losses.[11] Indeed, manipulating multi-scale porosities and EM wave dissipating factors can lead to a potent lossy medium with minimal impedance mismatching. Controlling the impedance mismatching enables suppressing the primary surface reflections, allowing the penetration of EM waves into the shielding construct.[2,12] In pursuit of this objective, aerogels have emerged as promising contenders for generating absorption-dominant shielding structures, owing to their plentiful porosity and the potential for a porous, electrically conductive/magnetic hierarchical arrangement that coexists with exceptional lightness.[11] Nevertheless, a common drawback among many aerogels lies in their inherent rigidity, and poor structural integrity, which collectively limits their functional versatility.[13]

Thus far, a plethora of strategies have emerged to develop absorption-dominant shielding constructs aimed at effectively attenuating EM waves and minimizing surface reflections by addressing impedance mismatching. These strategies encompass a range of approaches, including the implementation of gradient electrical conductivity,[14] the utilization of multilayered structures featuring alternating magnetic/conductive layers,[15] the generation of foams and aerogels as highly effective porous mediums,[16,17] structured Janus aerogels,[18] liquid-templating aerogels generation approach,[19] engineerable bridge micro-capacitance-based shielding constructs,[20] hydro-, organo-, or iono-gel absorbers,[12] metal–organic-framework (MOF)-based EM waves attenuating structures,[21–23] and hybrid shielding constructs featuring a combination of EM waves dissipating components.[24] Regardless of the advancement in these methodologies, the emphasis has primarily been on the structural aspects, neglecting the importance of blocking induced reflections from metallic parts, which are integral components of most advanced technological equipment.

Despite the recent progress in developing porous EMI shielding constructs, the capability of proposed methods in generating a versatile and superior absorption dominant shielding structure with controllable features is still limited.[1,2] Addressing this challenge passes through the art of interfacial complexation, a process that facilitates the organization of functional nanoparticles at the interface of two immiscible liquids through electrostatic interaction with a ligand. This interaction results in the jamming of nanoparticles at the interface, leading to the formation of nanoparticle surfactants. These unique nanoparticle surfactants contribute to the development of a robust solid interfacial layer, preserving the three-dimensional structure of liquid constructs while mitigating potential instabilities.[25] The resulting 3D-structured liquid constructs serve as templates for the generation of aerogels. The highly controllable nature of this process, combined with various adjustable parameters, allows for the deliberate engineering of templates before the freezing and lyophilization stages. This exceptional level of control in assembly and structuring through interfacial complexation empowers the manipulation of aerogel characteristics, making it possible to tailor them for highly effective absorption-dominant shielding systems.[19]

Herein, the challenge associated with the induced EM pollution by the metallic substrates was addressed by employing the art of interfacial complexation, allowing the engineering of shielding structures from nano-scale chemistry and micro-scale assembly of nanoparticles (NPs) to bulk manufacturing of multi-scale porous constructs.[19] Leveraging the synergistic interplay between 2D graphene oxide (GO) flakes and 1D cellulose nanofiber (CNF) within liquid templates for aerogel fabrication allows increasing intra- and inter-filament porosities per volume of aerogel through precise compositional and processing adjustments. This approach promotes electron migration and hopping by forming conductive networks that bridge reduced GO and CNF, optimizing the material's electrical properties. This enhances the internal scattering and conduction loss, intensifies the EM waves dissipating factors, and as a result, leads to an absorption dominant shield with controlled surface reflections. At the same time, such synergy promotes the structural integrity and elastic resilience of aerogels, making them a potent mechanically robust porous medium as a barrier against the induced reflections of other reflective substrates, *e.g.*, highly conductive metallic substrates.

Employing the concept of interfacial complexation, we addressed a potential drawback of reflection-dominant shielding systems by coining an anti-reflection aerogel termed 'aerogel electromagnetic traps'. When paired with metallic substrates, aerogels effectively block the incident EM waves and reflections from superconductive metals such as aluminum (Al), titanium (Ti), copper (Cu), and carbon-coated alumi-

Mohammad Arjmand

Dr Mohammad Arjmand is a leading and award-winning researcher in the areas of nanotechnology and polymer science and engineering. Dr Arjmand is a faculty member (since 2018) at the University of British Columbia, Okanagan campus (UBCO). He is also a Canada Research Chair in Advanced Materials and Polymer Engineering and the lead of the Plastic Recycling Research Cluster at UBCO. Dr Arjmand directs Nanomaterials and Polymer Nanocomposites Laboratory (NPNL), which focuses on the synthesis and engineering of multifunctional nanomaterials and polymer nanocomposites. Prior to joining UBCO, Dr Arjmand was a postdoctoral fellow at the Universities of Calgary and Toronto.

num (C–Al), altering their shielding mechanism to absorption dominant. The absorption dominant aerogel-metal shields showed total shielding effectiveness (SE_T) and absorbance (A) of 58–89 dB and 0.70–0.81, respectively. The presented anti-reflection concept herein could bring a vast range of opportunities to resolve the traditional drawback of metallic shields to tackle the challenges of sensitive electronics.

2. Materials and methods

2.1. Materials

This research employed analytical-grade reagents to synthesize the nanomaterials. Accordingly, to produce graphene oxide (GO), H_2SO_4 (98%), H_3PO_4 (85%), $KMnO_4$, H_2O_2 (30%), HCl (37%), and ethanol (anhydrous with ≤0.003% H_2O) were used, all supplied by Sigma-Aldrich. The large graphite flakes were supplied by Asbury Carbons. To synthesize cellulose nanofiber (CNF), NaBr, NaOH, NaCIO, and 2,2,6,6-tetramethyl-1-piperidinyloxy (TEMPO) were supplied by Sigma-Aldrich. The bleached and refined eucalyptus kraft pulp with 2 wt% solid concentration was utilized as the source of cellulose. In all of the stages of the synthesis procedures, highly pure deionized (DI) water with a resistivity of 18.2 MΩ was used, generated *via* ELGA model MEDICA EDI 15/30. The PSS-[3-(2-aminoethyl) amino]propyl-heptaisobutyl substituted (POSS) as the ligand and hexane (97%) as the extrusion medium were supplied by Sigma-Aldrich.

2.2. Methods

2.2.1. Nanomaterials synthesis. The synthesis of GO was carried out *via* the exfoliation of graphite flakes using the improved Hummers' method[26] with slight modifications according to our previous protocols.[11,19] The purified and concentrated GO paste with a concentration of 10 mg mL^{-1} was kept in a sealed container and used for the preparation of dilutions. The cellulose nanofibers synthesis and their TEMPO-mediated oxidation process were performed according to our previous study,[19] using refined bleached eucalyptus kraft pulp as the cellulose source. Detailed experimental steps for synthesizing GO and TEMPO-oxidized CNF are provided in the ESI.†

2.2.2. Aerogel production. The aerogels were produced by lyophilizing the frozen liquid templates. Accordingly, first, the inks were prepared with the desired concentrations and composition. As such, the GO and GO : CNF (1 : 1 weight ratio) inks were prepared at 0.5 and 1 wt% concentrations upon mixing the proper amount of GO and/or CNF, followed by 3 h stirring and 10 min bath sonication. The inks were thence loaded in a syringe equipped with the desired needle size and placed in an extrusion printing machine supported with an automatic pressure adjustment unit (Allevi 2 3D bioprinter). The liquid templates were prepared upon injection of the uniformly dispersed inks into the extrusion medium composed of 1 wt% POSS within the hexane at the pressure of 10–15 psi. Upon the injection of ink into the POSS-hexane domain, the POSS mole-

cules diffuse into the interface and electrostatically interact with the deprotonated carboxylic acid functional groups of GO and/or CNF through protonation of their amine groups ($-NH_3^+$). This electrostatic bonding at the interface leads to the formation of nanoparticle surfactant (NPS), locking in the non-equilibrium shape of filamentous threads of GO or GO : CNF and avoiding their breakup into discrete droplets by suppressing the instabilities.[19] Next, the formed liquid templates were frozen at −85 °C within an ultra-low temperature freezer for 24 h, then the POSS-hexane extrusion medium was decanted away, and finally, the frozen templates were lyophilized in a freeze drier (LABCONCO 4.5 L benchtop freeze dryer). This process leads to free-standing filamentous aerogels composed of core–shell filaments with a thin solid skin wrapped around a porous core.

For the reduction of aerogels, neat GO and/or GO–CNF aerogels were placed in the tube furnace (Across International) and annealed at 800 °C for 1 h under Ar, leading to the formation of reduced GO and GO–CNF aerogels (rGO and rGO–CNF). The density of the aerogels before and after the reduction processes was analyzed by measuring the volume and weight of five aerogel samples and reporting the average values (density: ρ = weight (g)/volume (cm^3)). Of note, the frozen templates were washed several times with fresh hexane to remove any remnants of POSS or impurities on the surface of the samples prior to lyophilization. For assessing the shielding parameters, the liquid templates were generated with 27 (inner diameter (I.D.) 0.21 mm) and 15 (I.D. 1.372 mm) needle gauges to tune the diameter of the filaments after lyophilization.

For shielding assessments, the aerogels were molded in 25 mL beakers with an inner diameter of 32.6 mm. The aerogels were generated at different thicknesses (2, 4, and 6 mm) to assess the effect of thickness on their total shielding effectiveness.

2.3. Characterization

The synthesized nanomaterials and generated aerogels were characterized *via* diverse techniques. Accordingly, the Fourier-transform infrared spectroscopy (FTIR) (Nicolet-S20) was used to assess the functionality of nanomaterials. Micro Raman spectroscopy (Brucker Senterra II) equipped with an Olympus U-TV1X-2 microscope was used to assess the D-band, G-band, and structural defects of resulting non-reduced and reduced aerogels. Likewise, the X-ray diffractogram setup (Brucker D8 Advance) was employed to assess both nanomaterials and aerogels. In this equipment, the X-ray is generated *via* a copper anode with $K\alpha_1$ = 1.540 60 Å, $K\alpha_2$ = 1.544 39 Å, and $K\beta_1$ = 1.392 22 Å, and Ni Kβ is employed as the filter. The scattered X-rays from the samples were collected *via* an Eiger2R 500K detector. The height and position of the samples were manually calibrated using a twin laser system assembled on the diffractometer. The aerogel samples were assessed *via* the parallel beam technique because of their uneven surface and abundant porosities.

The morphology of nanomaterials and aerogels was assessed with a field emission scanning electron microscope

(FESEM) (Tescan Mira 3 XMU). The elemental distribution of nanomaterials was analyzed through an assembled Oxford Instruments X-Max energy dispersive spectrometer (EDS) detector on the FESEM. GO samples were analyzed with high-resolution transmission electron microscopy (HRTEM) (80-300 Titan LB) to ensure their exfoliation with the desired quality.

The dynamic interfacial tension (IFT) assays were performed by holding 5 μL of aqueous inks against the hexane domain with and without POSS molecules using Biolin Scientific Theta Flow. The contraction tests were conducted by injecting an aqueous droplet of the ink in the non-polar domain with and without POSS to witness the wrinkles as proof of nanoparticle jamming. The electrical conductivity of the reduced aerogels was measured using a Loresta GP resistivity meter (Mitsubishi Chemical Co. model MCP-T700). A universal tensile machine (Z010 Zwick/Roell) was employed to perform the cyclic compression tests using a 200 N load cell. The aerogel sample was analyzed at 20, 40, 60, 70, 80, and 90% compressive strains with a loading–unloading speed of 5 mm min^{-1}. The shielding parameters of reduced aerogels and paired ones with metallic substrates were analyzed using a vector network analyzer (VNA) (P9374A Keysight) in the X-band frequency range (8.2–12.4 GHz). Accordingly, the aerogels were sandwiched between waveguides, and exposed to EM waves, and thence their complex scattering (S-) parameters were collected. The scattering parameters were then used to measure the reflectance (R), absorbance (A), transmittance (T), reflection loss (SE_R), absorption loss (SE_A), total shielding effectiveness (SE_T), and specific shielding effectiveness (SSE/t). Detailed formulations and experimental steps for measuring the shielding parameters can be seen in the ESI.†

3. Results and discussion

Anti-reflection aerogels, namely "aerogel electromagnetic traps", were produced through engineering the assembly of nanoparticles at the interface of two immiscible liquids, *viz.*, interfacial complexation,[19] *via* pressure-adjusted extrusion of aqueous inks (herein, GO (0.5–1 wt%, 5–10 mg mL^{-1}) and GO:CNF (weight ratio 1:1, 0.5–1 wt%)) into the enriched hexane domain with POSS. Fig. 1(a) illustrates the method for yielding 3D-structured anti-reflection aerogels starting from (I) pressure-adjusted extrusion of the ink into the ligand (POSS)-oil (hexane) phase to form liquid templates and (II) freezing of the generated assemblies, to (III) lyophilization of liquid templates toward manufacturing (IV) multi-scale porous aerogels (Fig. 1(b)).

The fabricated filamentous aerogels offer a multi-scale porous framework with abundant engineerable inter-filament (macro-scale) and intra-filament (micro-scale) porosities (Fig. 1(c) and (d)), making it an ultra-lightweight construct with densities ranging between 5.39–5.96 and 3.12–3.40 mg cm^{-3} at non-reduced and thermally annealed states (Fig. 1(e)), respectively. This offers a significant advantage for applications that require porosity, such as EMI shielding. It ampli-

fies multiple internal scatterings of EM waves across various engineered interfaces, thereby greatly dissipating the electromagnetic waves.[2] Indeed, the back-and-forth reflections between impedance-mismatched interfaces, along with the EM wave dissipating features such as dielectric and conduction losses, turn the aerogel into a formidable trap for incoming electromagnetic waves.[2,19] As illustrated in Fig. 1(c) and (d), the bulk aerogels consisted of abundant entangled core–shell filaments that formed a well-defined 3D structure. The aerogel's core–shell filaments comprised a solid thin tubular skin made of nanoparticle surfactants and a porous core derived from the hierarchical arrangement of reduced GO (rGO) flakes integrated with carbonized CNF (rGO–CNF). The nanoparticle surfactants are the product of the electrostatic interaction of nanoparticles and ligands (POSS) at the interface of the two immiscible liquids (water/hexane), preserving the non-equilibrium shape of liquid filaments by overcoming the instabilities (see ESI† for detailed explanation and evidence).[19]

The rGO–CNF aerogel showcases superb reversible compressibility, capable of undergoing 90% compressive strain and recovering its shape quickly after force release because of its high elastic resilience (Fig. 1(f)). Such excellent mechanical integrity roots from the unique core–shell morphology of aerogel's filaments, capable of withstanding high compressive strains.[19] The versatility and swift shape recovery, combined with the adaptable nature of the process, make these developed aerogels highly manageable, positioning them ideally for advanced applications. Indeed, many aerogels exhibit inadequate mechanical performance, constraining their use in various applications. Furthermore, adjusting the gauge number of the injection needle, transitioning from 15 (inner diameter (I.D.) of 1.37 mm) to 27 (I.D. of 0.21 mm), results in a shift in the average filament diameter from 491 ± 34 μm to 169 ± 19 μm following lyophilization of the liquid templates. This alteration amplifies interacting interfaces and multi-scale porosities per volume within the aerogel (see Fig. 1(g and h) and Fig. S7†). Consequently, there is an increase in the number of porosities and spacings between filaments, facilitating the back-and-forth reflections of EM waves between interfaces and enhancing energy dissipation. Additionally, increasing the concentration of the GO:CNF ink (maintaining a 1:1 weight ratio) from 5 mg mL^{-1} to 10 mg mL^{-1} significantly enhances the micro-scale porosities per volume within the filament and reduces the average pore size from 58.01 ± 17.55 to 41.13 ± 15.47 (Fig. S8†). This demonstrates the tunable nature of the approach in engineering multi-scale porosities within the aerogels, thereby bolstering the trapping and dissipation of EM waves across numerous interfaces. This holds significant potential for applications like EM shielding. The EM waves are trapped amidst the induced porosities, leading to a sequential of reflections between the filaments (macro-scale porosities) and further internal reflections within the filament's porous core (micro-scale porosities), effectively converting the EM waves into heat. Detailed characterizations of the synthesized nanomaterials, liquid templates, and aerogels can be found in the ESI.†
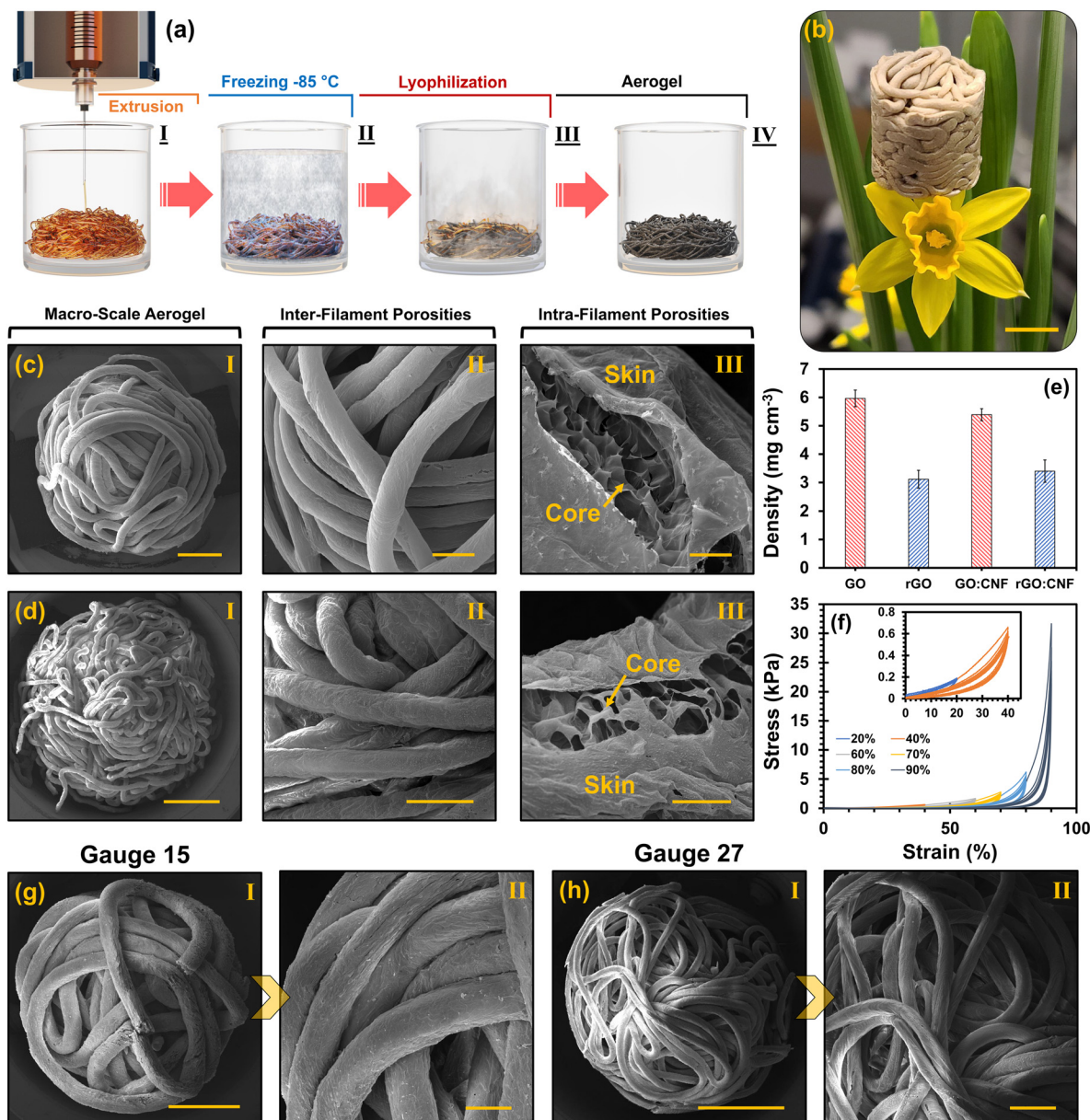
Fig. 1 (a) Yielding free-standing filamentous aerogels through interfacial complexation; (I) pressure-adjusted extrusion of either GO or GO : CNF ink into the POSS-hexane domain to generate liquid templates, (II) freezing of the formed filamentous liquid template at −85 °C, (III) lyophilization of the frozen assemblies, and (IV) formation of 3D-structured aerogels. (b) Ultra-lightweight GO aerogel on a light leaf of a daffodil; scale bar is equal to ~13.39 mm, of note this image is taken by a digital camera and the scale bar is approximate. FESEM images of (c) rGO and (d) rGO–CNF aerogels; sub-parts showing (I) bulk aerogel construct, (II) macro-scale porosities between filaments (inter-filament porosities), and (III) micro-scale porosities within the filaments (intra-filament porosities); scale bars correspond to (I) 2 mm, (II) 1 mm, and (III) 100 μm. (e) The density of the aerogels before and after the thermal annealing (800 °C, 1 h under Ar). (f) The stress−strain curve of rGO–CNF aerogels at different compressive strains, *i.e.*, 20 to 90%, with six compression cycles at each strain. FESEM images of the 3D-structured filamentous GO−CNF aerogels extruded by needles with gauge numbers (g) 15 (inner diameter (I.D.) of 1.37 mm) and (h) 27 (I.D. of 0.21 mm). Scale bars are equal to (g & h) (I) 2 mm and (II) 500 μm.

The electrical conductivity of the aerogel, as an essential character of any shield, was promoted from 11.43 S m^{-1} for rGO aerogel to 35.63 S m^{-1} for carbonized rGO–CNF aerogel (Fig. 2(a)). Importantly, maintaining the aerogels' electrical conductivity at a controlled level can reduce the initial surface reflections. This allows the EM waves to penetrate and become effectively trapped within the shield.[1]

Fig. 2(b and c) and S11–S12† demonstrate the shielding effectiveness and shielding coefficients of the rGO–CNF aerogels at different ink concentrations (0.5 and 1 wt%) and thicknesses (2, 4, and 6 mm). As evidenced, the rGO–CNF aerogels prepared with an ink concentration of 0.5 wt%, extruded with a gauge 27 needle, showcased a SE$_T$ ranging from 19 dB to 31 dB for aerogels with 2 to 6 mm thicknesses with an absorption
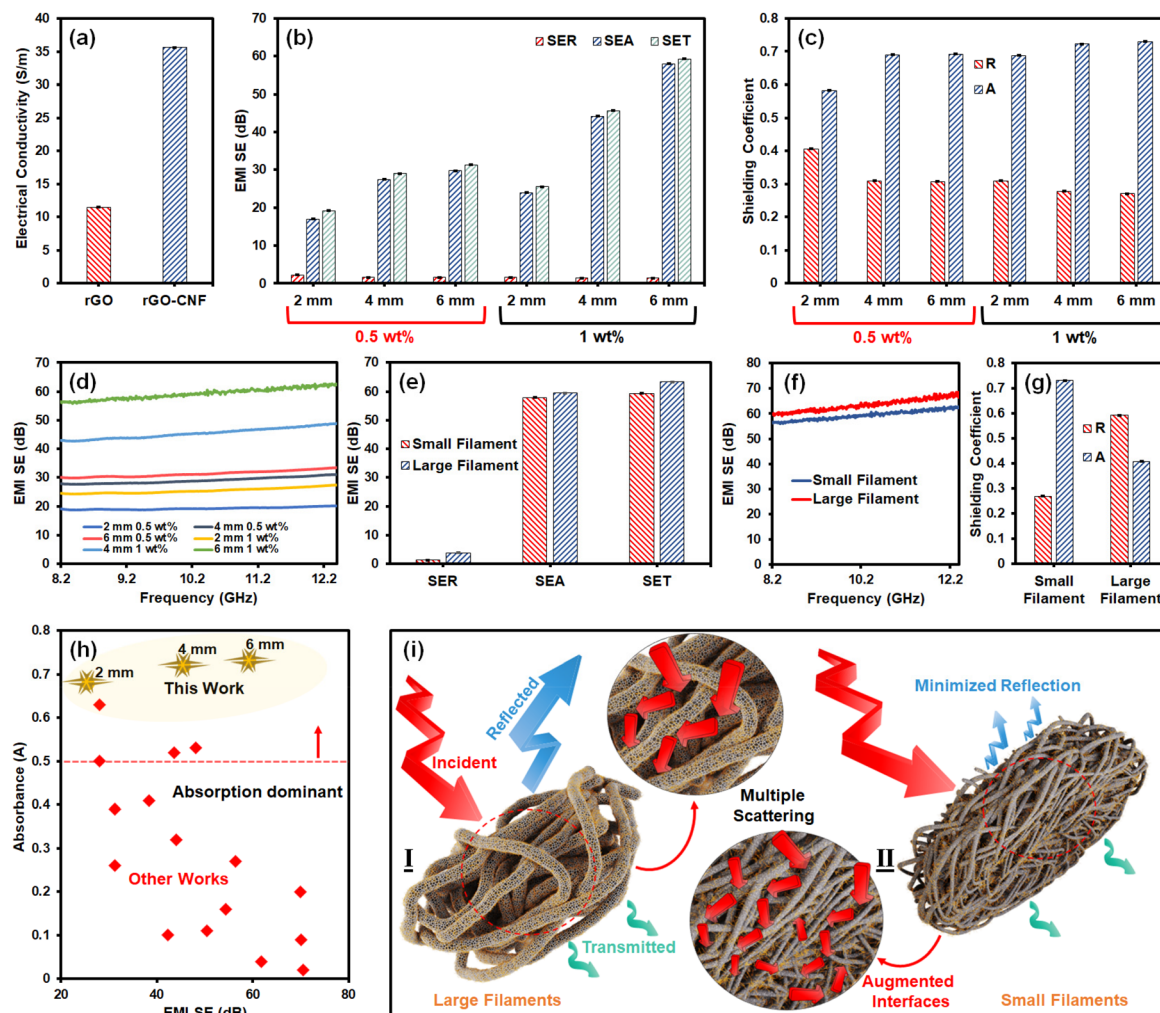
Fig. 2 (a) The electrical conductivity of the rGO and rGO–CNF aerogels. (b) The EMI shielding and (c) shielding coefficients of rGO–CNF aerogels at different ink concentrations (0.5 and 1 wt%) and thicknesses (2–6 mm). (d) The frequency-dependant EMI shielding of rGO–CNF aerogels over the X-band frequency range (8.2–12.4 GHz). Comparing small-sized and large-sized filament aerogels, including (e) EMI shielding and shielding parameters, (f) frequency-dependant EMI shielding over the X-band frequency range, and (g) shielding coefficients. (h) The absorbance (*A*) of the rGO–CNF aerogel (1 wt% ink, gauge 27, *i.e.*, small-sized filaments) at different thicknesses compared with previously developed foams and aerogels; the corresponding data can be seen in Table S1.† (i) The shielding mechanism of rGO–CNF aerogels with (I) large and (II) small filaments. As illustrated, declining the diameter of the filament in rGO–CNF aerogels increases the number of interfaces and porosities per volume of the aerogel, increasing the equivalent impedance and thereby minimizing the surface reflection. This alters the nature of the shield from dominant reflection to absorption.

dominant shielding characteristic (absorbance of 0.58–0.69 and absorption loss (SE$_A$) of 16.92–29.76). Similarly, a slight increase in the ink concentration to 1 wt% considerably boosted the SE$_T$ to 25.54–59.32 dB for aerogels with thicknesses 2 to 6 mm with a stronger absorption dominant characteristic (absorbance of 0.68–0.73 and SE$_A$ of 23.91–57.94). Additionally, the frequency-dependent EM shielding (Fig. 2(d)) showed a stable EMI shielding over the whole X-band frequency range (8.2–12.4 GHz), indicating the strong shielding performance of the filamentous aerogels.

Interestingly, experimental assessments revealed that tuning the diameter of the filamentous aerogels by changing the needle gauge during extrusion could alter the shielding characteristic of the aerogels. In this regard, two different

types of filamentous aerogels were prepared with needle gauges of 27 and 15, denoted as small and large filaments. Both aerogels with small and large filaments exhibit strong SE$_T$ values of 59.32 and 63.39 dB (Fig. 2(e) and Fig. S13†), respectively, with a nearly stable uprising frequency-dependant EMI SE over the whole X-band frequency range (Fig. 2(f)). The aerogel with a smaller filament size (injection needle gauge 27) showed an absorption-dominant shielding behavior (absorbance of 0.73 and SE$_A$ of 57.94 dB), while increasing the filament size (injection needle gauge 15) altered the shielding character to reflection-dominant (absorbance of 0.40 and SE$_A$ of 59.47 dB) (Fig. 2(g)). This discrepancy arises due to the presence of broader impedance mismatched surfaces in aerogel, characterized by larger filaments and significantly fewer poros-

ities. This configuration leads to increased scattering of EM waves, primarily in the form of reflection. The underlying mechanism involves the enforced oscillation of free charge carriers on the shield's surface, which prevents the penetration of EM waves into the aerogel. Consequently, this configuration hinders the further dissipation of these waves.[1] Whereas, in aerogel with smaller filaments, soaring in the volume of porosities increases the equivalent impedance and declines the surface reflection.[27] This allows the EM waves to penetrate the shield and be dissipated when facing numerous interfaces in the porous core of the aerogel filaments. Of note, a porous material's equivalent impedance ranges between its components' impedance, *i.e.*, free space and conductive scaffold. Devising a higher equivalent impedance, *i.e.*, a closer resemblance to the impedance of free space (377 Ω), allows EM waves to penetrate the structure with reduced reflections.[27]

Moreover, thanks to lightness, abundant porosities, and high ohmic loss, both aerogels with small and large filaments offer remarkable specific shielding effectiveness (SSE/t) of 35 218 and 32 691 dB cm^2 g^{-1}, respectively. Compared with the recent practices in the field (Fig. 2(h) and Table S1†), the small filament aerogels can offer high shielding effectiveness at one of the lowest ink concentrations (0.5–1 wt%) or densities with an absorption-dominant shielding character.

The exceptional shielding performance of the filamentous aerogels can be attributed to their distinct multi-scale porous architecture. As depicted in Fig. 2(i), when EM waves strike the aerogel, a series of interactions occur: a portion of the incident EM waves reflect off the aerogel surface in the form of a scattered field, which was minimized by increasing the equivalent impedance. This allows penetration into the shield where the EM waves trapping and the main dissipation occur. Reflections recur between the filaments because of their macro-scale porosity. This is accompanied by scattering at the interface of the solid exterior and porous core, with additional internal scattering taking place within the filaments' micro-scale porosities. These interactions result in a significant reduction of the EM waves' energy. As a result, the energy from these waves is converted into heat due to the high kinetic energy of mobile charge carriers vibrating at elevated frequencies,[27] leading to highly effective shielding with a predominantly absorptive characteristic. It's noteworthy that, as per the data gathered, the diameter of the filaments is instrumental in this absorption-dominant shielding.

These coined aerogel EM traps with minimized surface reflection and a multi-scale porous lossy medium for EM waves can be used as a potent barrier against the induced secondary EM pollution of metallic shields or even the metallic parts of sensitive electronics.[1] When paired with metallic substrates, these aerogels are capable of shifting the shielding mechanism of metals from predominantly reflective ($R > 0.8$) to notably absorptive ($A > 0.7$). Fig. 3(a) showcases the anti-reflection character of rGO–CNF aerogels when paired with metallic substrates (Fig. 3(a)I–II). The anti-reflection property of the produced aerogels originates from their potent lossy medium coupled with a controlled electrical conductivity.

Choosing a finite electrical conductivity ensures that EM waves can penetrate the aerogel's EM trap with reduced surface reflections. However, an unchecked increase in electrical conductivity can give rise to induced reflections, as this is primarily a surface phenomenon.

Furthermore, the vast array of interfaces and porosities in multi-scale porous aerogels, such as those between filaments, between the filament's outer layer and its porous core, and within the micro-scale porosities of the tubular core, greatly enhance multiple reflections and internal scatterings (as depicted in Fig. 3(a) parts II–III). This significantly contributes to creating a powerful medium for trapping and attenuating EM waves. By optimizing these multi-scale porosities and amplifying both interfacial/dipole polarization and conduction loss, one can more effectively dissipate incoming EM waves, capitalizing on the cumulative effect of multiple scatterings.[28–30]

Furthermore, the stacking of rGO flakes and their intimate interactions with carbonized CNFs or other rGO flakes result in interfacial polarization at contact sites plus dipole polarization at localized defective areas when exposed to alternating electromagnetic fields, promoting the loss of EM waves, as illustrated in Fig. 3(a)IV. In this context, the one-dimensional (1D) carbonized CNFs serve as connective bridges to the two-dimensional (2D) rGO flakes. This synergy creates a conductive network facilitating electron migration and hopping, which in turn contributes to conduction losses and helps dissipate the energy of the EM waves, as depicted in Fig. 3(a)V.[31] Notably, the defective sites in the stacked rGO sheets promote polarization loss, benefiting the dissipation of EM waves.[32,33] Importantly, when the EM waves strike the metallic substrate at the back of the aerogel EM trap, the EM waves reflect back and dissipate in the lossy medium of the aerogel trap. This blocks the induced secondary EM pollution of metallic substrates as one of the most important challenges of shielding science and sensitive electronics.

As a proof of concept, a 6 mm thick rGO–CNF aerogel (1 wt%, gauge 27) was paired with Al foil (thickness (t): 15 μm), carbon-coated Al (C–Al) foil (t: 15 μm), Cu foil (t: 10 μm), Cu tape (t: 50 μm), Ti foil (i: 20 μm), Ti mesh (t: 426 μm), and Zn foil (t: 106 μm), and the EMI shielding parameters and shielding coefficients were recorded. All the employed thin metallic substrates standalone showcased a reflection dominant shielding character with reflectance (R) and SE$_T$ of 0.88–0.98 and 30.08–48.25 dB, respectively (Fig. S14, 15 and Table S2†). Upon pairing the metallic substrates with anti-reflection ultra-lightweight filamentous rGO–CNF aerogel, the nature of all shielding systems changed from reflection dominant to totally absorption dominant with absorbance (A), SE$_A$, and SE$_T$ of 0.70–0.81, 57.98–88.11 dB, and 58.85–89.32 dB, respectively (Fig. 3(b and c) and Table S3†). Additionally, the rGO–CNF aerogel (Fig. 3(d)) and paired metallic substrates with anti-reflection aerogel (Fig. 3(e)) showcased superior shielding effectiveness with significantly minimized reflection loss (SE$_R$), over the whole X-band frequency range (8.2–12.4 GHz).
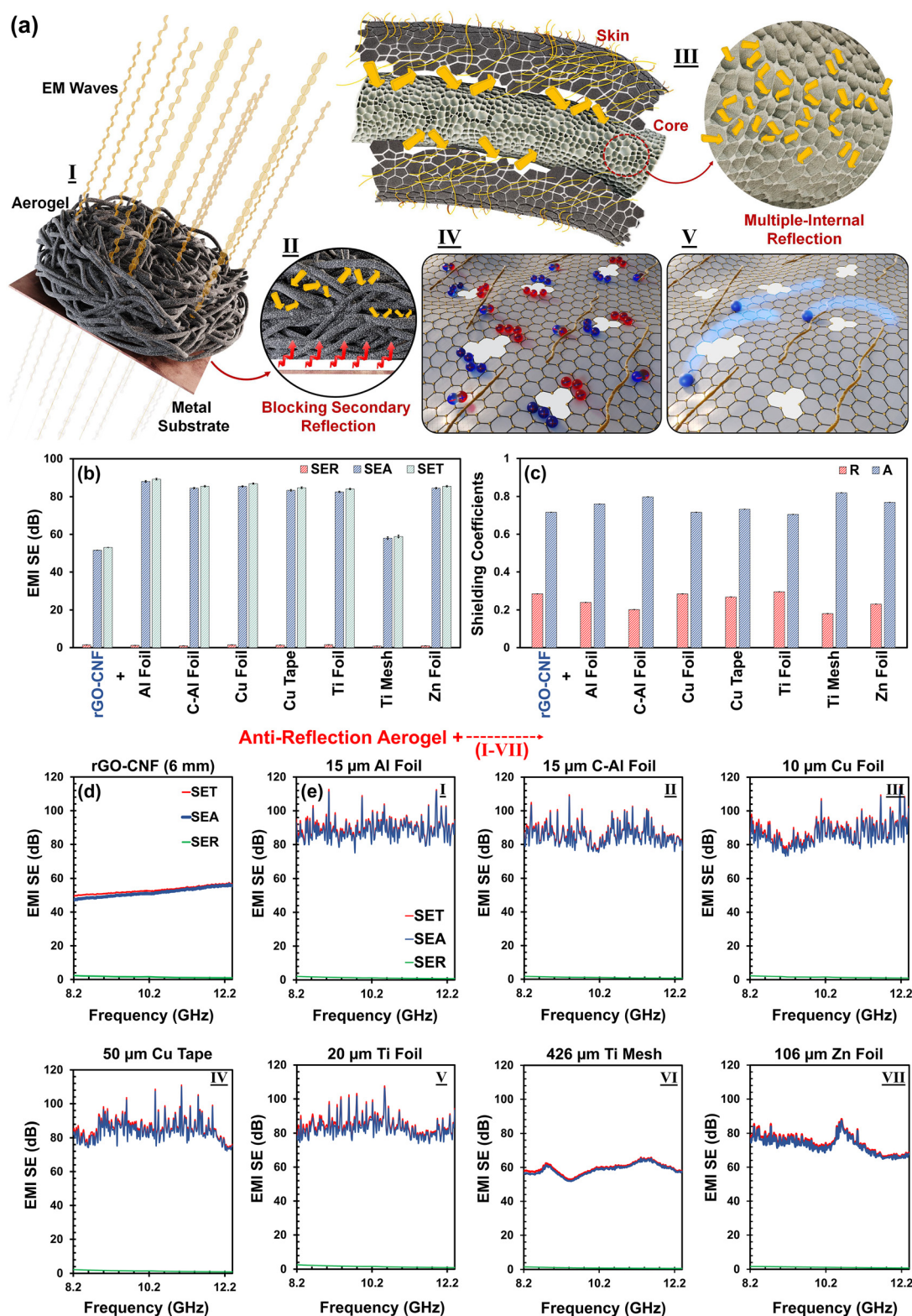
Fig. 3 (a) Aerogel EM trap's mechanism of action, including (I) their pairing with superconductive metallic substrates, (II) blocking the induced reflections, *i.e.*, secondary EM pollution, of metallic substrates and multiple reflections among inter-filament porosities, (III) interaction of EM waves with intra-filament porosities, including the multiple reflections between the skin and core of the core–shell filaments and multiple internal reflections within the porosity of the tubular porous core of aerogel's filaments, (IV) interfacial and/or dipole polarization losses, and (V) conduction loss as a result of electron migration and hopping. The golden rods in parts IV and V represent the CNF, while blue and red spherics show positive and negative charges. (b) The EMI SE, and (c) the shielding coefficients of 6 mm thick rGO–CNF aerogels (1 wt%, gauge 27) with and without thin metallic foils/tape cover. EMI SE of the (d) rGO–CNF aerogels without any back cover and with (e) (I) 15 μm Al foil, (II) 15 μm carbon coated Al foil (C–Al foil), (III) 10 μm Cu foil, (IV) 50 μm Cu tape, and (V) 20 μm Ti foil, (VI) 426 μm Ti mesh, and (VII) 106 μm Zn foil within the X-band frequency range.
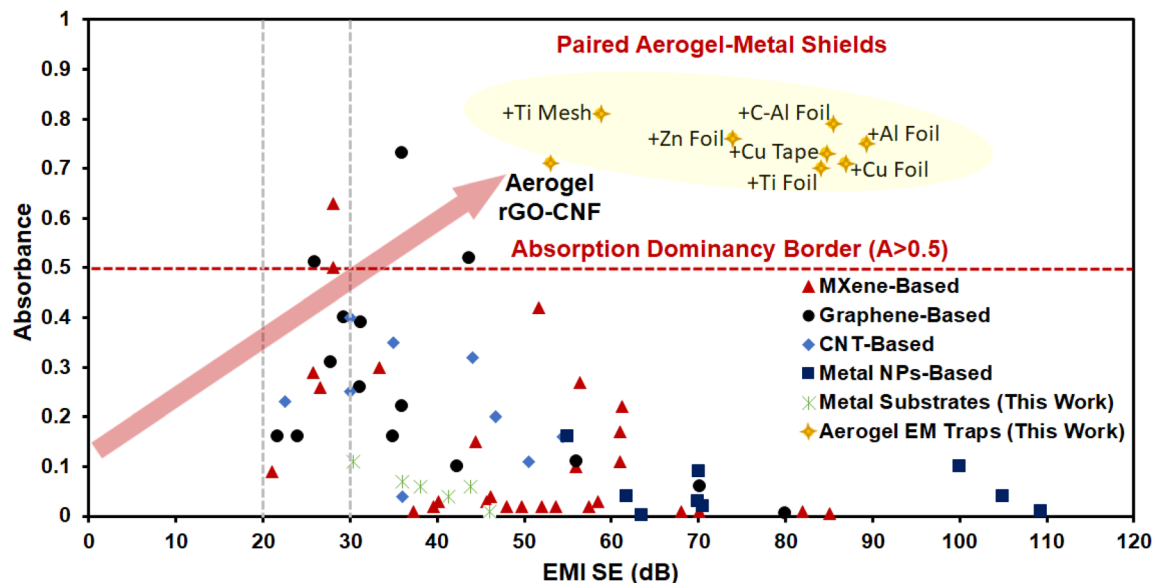
Fig. 4 The EM shielding performance of developed anti-reflection aerogels paired with metallic substrates compared with recent practices in the field; corresponding data can be seen in Table S4.†

The proposed "aerogel electromagnetic trap" approach provides an efficient aerogel framework capable of effectively minimizing the surface reflection, dissipating the intruding EM waves in their multi-scale porous lossy medium, and blocking the induced EM pollution of metallic substrates when paired with them. This paired aerogel-metal system establishes a new benchmark in absorption-dominant shielding designs, positioning it as one of the best practices in the field (Fig. 4 and Table S4†).

4. Conclusions

In our research, we introduce a versatile strategy for trapping and dissipating electromagnetic (EM) waves, termed "aerogel electromagnetic traps". This approach involves utilizing liquid templating of GO : CNF ink to produce filamentous multi-scale porous aerogels. These aerogels offer a solution to a significant challenge in shielding science, namely the reflection dominant nature of metallic EM shields plus their induced secondary EM pollution, when paired with metallic substrates. The key to unlocking this potential lies in the engineered porosity of the aerogel, which can be tailored across multiple scales as needed. By adjusting the porosity and filament size, we can minimize surface reflections and increase the number of interfaces for dissipating EM waves. This transformation shifts the aerogel's shielding nature from being predominantly reflective to absorptive. The resulting absorption-dominant shielding systems effectively trap EM waves, attenuate incident waves, and block reflections from metallic substrates. When paired with metallic substrates, these systems exhibit superior absorption dominant (A: 0.70–0.81) shielding effectiveness with a substantial SE_T of 58–89 dB. The pronounced anti-reflection properties of these ultra-lightweight aerogels hold promise for addressing longstanding challenges in shielding science. Our

innovation opens avenues for enhancing the efficiency of metallic shields by transitioning them to primarily operate through absorption-dominant shielding mechanisms.

Data availability

All the experimental data of this manuscript (including the excel file of raw data) plus supporting characterizations are provided in the attached ESI files.†

Conflicts of interest

There are no conflicts to declare.

Acknowledgements

References

1 S. A. Hashemi, A. Ghaffarkhah, E. Hosseini, S. Bahrani, P. Najmi, N. Omidifar, S. M. Mousavi, M. Amini,

M. Ghaedi, S. Ramakrishna and M. Arjmand, *Matter*, 2022, **5**, 3807–3868.

2 M. Panahi-Sarmad, S. Samsami, A. Ghaffarkhah, S. A. Hashemi, S. Ghasemi, M. Amini, S. Wuttke, O. Rojas, K. C. Tam, F. Jiang, M. Arjmand, F. Ahmadijokani and M. Kamkar, *Adv. Funct. Mater.*, 2023, 2304473.

3 D. Wanasinghe and F. Aslani, *Composites, Part B*, 2019, **176**, 107207.

4 X. X. Wang, Q. Zheng, Y. J. Zheng and M. S. Cao, *Carbon*, 2023, **206**, 124–141.

5 R. Kumar, S. Sahoo, E. Joanni, R. K. Singh, W. K. Tan, K. K. Kar and A. Matsuda, *Carbon*, 2021, **177**, 304–331.

6 J. Kruželák, A. Kvasničáková, K. Hložeková and I. Hudec, *Nanoscale Adv.*, 2021, **3**, 123–172.

7 J. Liu, L. Mckeon, J. Garcia, S. Pinilla, S. Barwich, M. Möbius, P. Stamenov, J. N. Coleman and V. Nicolosi, *Adv. Mater.*, 2022, **34**, 2106253.

8 A. Iqbal, P. Sambyal and C. M. Koo, *Adv. Funct. Mater.*, 2020, **30**, 2000883.

9 Y. Zhang, K. Ruan, K. Zhou and J. Gu, *Adv. Mater.*, 2023, **35**, 2211642.

10 B. Zhao, M. Hamidinejad, S. Wang, P. Bai, R. Che, R. Zhang and C. B. Park, *J. Mater. Chem. A*, 2021, **9**, 8896–8949.

11 A. Ghaffarkhah, S. A. Hashemi, S. Rostami, M. Amini, F. Ahmadijokani, A. Pournaghshband Isfahani, S. E. Mhatre, O. J. Rojas, M. Kamkar, S. Wuttke, M. Soroush and M. Arjmand, *Adv. Funct. Mater.*, 2023, 2304748.

12 Z. Zhao, L. Zhang and H. Wu, *Adv. Mater.*, 2022, **34**, 2205376.

13 K. Y. Lee, D. B. Mahadik, V. G. Parale and H. H. Park, *J. Korean Ceram. Soc.*, 2020, **57**, 1–23.

14 A. Sheng, W. Ren, Y. Yang, D. X. Yan, H. Duan, G. Zhao, Y. Liu and Z. M. Li, *Composites, Part A*, 2020, **129**, 105692.

15 M. Amini, M. Kamkar, F. Rahmani, A. Ghaffarkhah, F. Ahmadijokani and M. Arjmand, *ACS Appl. Electron. Mater.*, 2021, **3**, 5514–5527.

16 G. Y. Yang, S. Z. Wang, H. T. Sun, X. M. Yao, C. B. Li, Y. J. Li and J. J. Jiang, *ACS Appl. Mater. Interfaces*, 2021, **13**, 57521–57531.

17 T. Zuo, W. Wang and D. Yu, *J. Alloys Compd.*, 2023, **966**, 171644.

18 A. Ghaffarkhah, S. A. Hashemi, F. Ahmadijokani, M. Goodarzi, H. Riazi, S. E. Mhatre, O. Zaremba, O. J. Rojas, M. Soroush and T. P. Russell, *Nat. Commun.*, 2023, **14**, 7811.

19 S. A. Hashemi, A. Ghaffarkhah, M. Goodarzi, A. Nazemi, G. Banvillet, A. S. Milani, M. Soroush, O. J. Rojas, S. Ramakrishna, S. Wuttke, T. P. Russell, M. Kamkar and M. Arjmand, *Adv. Mater.*, 2023, **35**, 2302826.

20 P. Yan, H. Yujia, W. Qi, Z. Yong, H. Guangsu, R. Qichao and W. Jinrong, *Carbon*, 2020, **166**, 56–63.

21 P. Miao, N. Qu, W. Chen, T. Wang, W. Zhao and J. Kong, *Chem. Eng. J.*, 2023, **454**, 140445.

22 P. Miao, R. Zhou, K. Chen, J. Liang, Q. Ban and J. Kong, *Adv. Mater. Interfaces*, 2020, **7**, 1901820.

23 P. Miao, T. Zhang, T. Wang, J. Chen, T. Gao, Y. Wang, J. Kong and K. J. Chen, *Chin. J. Chem.*, 2022, **40**, 467–474.

24 L. Ma, L. Wei, M. Hamidinejad and C. B. Park, *Mater. Horiz.*, 2023, **10**, 4423–4437.

25 S. Shi and T. P. Russell, *Adv. Mater.*, 2018, **30**, 1800714.

26 D. C. Marcano, D. V. Kosynkin, J. M. Berlin, A. Sinitskii, Z. Sun, A. Slesarev, L. B. Alemany, W. Lu and J. M. Tour, *ACS Nano*, 2010, **4**, 4806–4814.

27 A. Ghaffarkhah, M. Kamkar, Z. A. Dijvejin, H. Riazi, S. Ghaderi, K. Golovin, M. Soroush and M. Arjmand, *Carbon*, 2022, **191**, 277–289.

28 S. Wu, D. Chen, W. Han, Y. Xie, G. Zhao, S. Dong, M. Tan, H. Huang, S. Xu and G. Chen, *Chem. Eng. J.*, 2022, **446**, 137093.

29 Y. Li, F. Meng, Y. Mei, H. Wang, Y. Guo, Y. Wang, F. Peng, F. Huang and Z. Zhou, *Chem. Eng. J.*, 2020, **391**, 123512.

30 Y. Wang, X. Han, P. Xu, D. Liu, L. Cui, H. Zhao and Y. Du, *Chem. Eng. J.*, 2019, **372**, 312–320.

31 M. Li, F. Han, S. Jiang, M. Zhang, Q. Xu, J. Zhu, A. Ge and L. Liu, *Adv. Mater. Interfaces*, 2021, **8**, 2101437.

32 X. Jian, B. Wu, Y. Wei, S. X. Dou, X. Wang, W. He and N. Mahmood, *ACS Appl. Mater. Interfaces*, 2016, **8**, 6101–6109.

33 B. Quan, W. Shi, S. J. H. Ong, X. Lu, P. L. Wang, G. Ji, Y. Guo, L. Zheng and Z. J. Xu, *Adv. Funct. Mater.*, 2019, **29**, 1901236.